

Effects of annealing atmosphere on defect-controlled ferromagnetism in Mn-doped β -Ga₂O₃

Xu Dai, Xi Zhang, Gang Xiang*

College of Physics, Sichuan University, Chengdu 610000, China.

*Corresponding email: gxiang@scu.edu.cn

Mn-doped β -Ga₂O₃ (GMO) thin films with room-temperature ferromagnetism are synthesized by polymer-assisted deposition and the effects of annealing atmosphere on their structures and physical properties are investigated. The characterizations show that the lattice constant, the concentrations of vacancy defects and the valence states of Mn dopants are all modulated by the annealing atmosphere. Notably, the samples annealed in air (GMO-air) exhibit a saturation magnetization as strong as 1.7 times that of the samples annealed in pure O₂ gas (GMO-O₂), which can be quantitatively explained by oxygen vacancy (V_O) defect-controlled ferromagnetism due to bound magnetic polarons established between the delocalized hydrogenic electrons of V_Os and local magnetic moments of various Mn ions (Mn²⁺, Mn³⁺, and Mn⁴⁺ ions) in the GMO thin films. Besides, the optical properties and electrical resistivity of the GMO films are also tuned by the annealing atmosphere. Our results provide insights into the defect-controlled ferromagnetism in Ga₂O₃ and suggest an alternative way for spintronic engineering of related materials.

I. INTRODUCTION

Owing to the co-existence of charge and spin degrees of freedom in the diluted magnetic semiconductors (DMSs), tremendous attention has been aroused in semiconductor spintronics [1-4]. As a promising wide-bandgap material for various applications including solar-blind detectors and high-frequency power devices, gallium oxide (Ga_2O_3) has attracted interest for its potentials in spintronic applications very recently [5-8]. It is found that the ferromagnetism in Ga_2O_3 can be realized by doping with various metallic elements, such as Fe [9], Ni [10], Cr [11], Sn [12] and Mn [13-18]. For instance, Ni-doped $\beta\text{-Ga}_2\text{O}_3$ nanoparticles with room-temperature ferromagnetism (RTFM) were synthesized by hydrothermal method, in which the ferromagnetism mainly came from the interaction between Ni^{2+} and O^{2-} ions and related defect contributions [10]. Peng *et al.* reported the coexistence of ferromagnetic and antiferromagnetic phases in the Mn-doped $\beta\text{-Ga}_2\text{O}_3$ prepared by ion implantation [13]. Pei *et al.* reported the RTFM of Mn-doped Ga_2O_3 and explained it using a carrier-mediated double exchange model [14]. Guo *et al.* found that both coercive field (H_C) and saturation magnetization (M_s) in Mn-doped $\beta\text{-Ga}_2\text{O}_3$ increased with Mn doping concentration, which could be explained by coupling between Mn ions and oxygen vacancies (V_{Os}) [15]. Huang *et al.* found that both Mn dopants and defects could affect the RTFM in Mn-doped $\beta\text{-Ga}_2\text{O}_3$ [16]. On the other hand, the calculations based on density functional theory (DFT) suggested that the RTFM of Mn-doped $\beta\text{-Ga}_2\text{O}_3$ came from the strong p - d coupling and the delocalization of O-2 p orbitals [17]. Obviously, although much work has been done on the fabrication and characterization of

ferromagnetic Ga_2O_3 , the mechanism underlying the ferromagnetism still remains controversial, especially the role of oxygen in the ferromagnetic ordering in Ga_2O_3 . Therefore, for both basic science and potential applications, it is important and necessary to further investigate the roles of oxygen and other structural factors on the ferromagnetism of Ga_2O_3 .

In this work, Mn-doped $\beta\text{-Ga}_2\text{O}_3$ (GMO) pre-films are first prepared by polymer-assisted deposition (PAD) and then annealed in air atmosphere and pure O_2 gas to obtain GMO-air and GMO- O_2 polycrystalline thin films, respectively. The structures of the obtained films are characterized and the effects of annealing atmosphere on the magnetic, optical, and electrical properties of the films are then investigated.

II. EXPERIMENTAL

The polyethyleneimine (PEI) ((M.W. 10,000, 99%, Sigma-Aldrich) and Ethylene Diamine Tetraacetic Acid (EDTA) (99.9%, Sigma-Aldrich) are added to deionized water in a certain proportion to prepare the polymer solution. Subsequently, gallium nitrate hydrate ($\text{GaN}_3\text{O}_9 \cdot x\text{H}_2\text{O}$, 99.9%, Sigma-Aldrich) is added to the polymer solution to obtain Ga-polymers solution, and manganese chloride tetrahydrate ($\text{MnCl}_2 \cdot 4\text{H}_2\text{O}$, 99.9%, Sigma-Aldrich) is added to the polymer solution to obtain Mn-polymers solution. Then the unbound ions need to be filtered out from the Ga-polymers solution and the Mn-polymers solution by Amicon cells. The Mn-doped Ga precursor (GaMn-polymers) solution is prepared by adding the Mn-polymers solution to the Ga-polymers solution, which is then dropped on single crystalline *c*-plane sapphire substrate to prepare pre-films using 30s-spin-coating at 3000 rpm. The GaMn-polymers

are tested by thermalgravimetric analysis and differential scanning calorimeter (TGA-DSC) (TA instruments, Q40) to study the changes of weight and calorie during annealing in air and pure O₂ gas. Fig. 1(a) shows the TG and DSC curves of the GaMn-polymers in air. The exothermic peaks at 290°C and 484°C represent the decompositions of the GaMn-polymers, and the endothermic peak at 588°C represents the crystallization of Mn-doped gallium oxide. The TG and DSC curves in pure O₂ gas show similar results. Based on the TG-DSC results, the pre-films are heated up to 550 °C for 1 h to completely decompose PEI and EDTA, and then annealed in air and pure O₂ gas at 750°C to obtain GMO-air and GMO-O₂ films, respectively. The annealing in oxygen-rich conditions is necessary for obtaining crystalline samples [19]. The digital photos of typical 2cm×2cm GMO-air and GMO-O₂ films in Fig. 1(b) show that the films are translucent brown. By changing the concentration of the precursor solution and the number of suspension coatings, dozens to hundreds of nanometer-thick GMO films are obtained. For comparison, undoped β-Ga₂O₃ films are also prepared.

The morphologies of the GMO films are depicted by atomic force microscope (AFM, Benyuan, CSPM5500). X-ray diffraction (XRD, Bruker D8, Empyrean analytical diffractometer) using a Cu Kα radiation source and high-resolution transmission electron microscopy (HRTEM, Titan Themes Cubed G2 300) are used to characterize crystalline structures. Cross-sectional samples for TEM are prepared by focus ion beam (FIB) milling in a Helios system (Tescan, LYRA 3 XMU). Elemental composition and valence are examined by X-ray photoelectron spectroscopy (XPS, Kratos AXIS Supra). Optical properties are evaluated using UV-visible spectrophotometer (PerkinElmer

Lambda 950 UV-Vis-NIR) and photoluminescence (PL, LS-45). Magnetic and electrical properties are measured by Superconducting Quantum Interference Devices (SQUID, Quantum Design, MPMS-XL-5) and four-probe resistivity tester (FPPRT, ST-2722), respectively.

III. RESULTS AND DISCUSSION

The three-dimensional AFM images indicate that the surface roughness of the GMO films is ~ 1.2 nm, as shown in Fig. 1(c). The crystal structures of the obtained translucent large-scale films are studied by XRD. As shown in Fig. 1(d), three diffraction peaks belong to (-201), (-402), and (-603) groups of the β -Ga₂O₃ are observed in all the samples, indicating the (-201) preferential growth orientation in the PAD films [20]. No peaks of Mn metal clusters, Mn oxides or compounds are found, which are consistent with the results of Mn-doped β -Ga₂O₃ in the literature [15-16]. Only one crystallization peak in the DSC curve of the GaMn-polymers also indicates the single crystal phase during annealing, as shown in Fig. 1(a). The inset is the enlarged view of θ -2 θ XRD patterns around 38°. Interestingly, comparing with those of un-doped β -Ga₂O₃, the diffraction peaks of GMO-O₂ are just slightly right-shifted, while the diffraction peaks of GMO-air are dramatically left-shifted. The (-402) inter-planar spacing values of un-doped, GMO-O₂ and GMO-air can be calculated using the Bragg equation and obtained as 0.232 nm, 0.230 nm and 0.240 nm, respectively. Since the size order of the cation radii in the GMO films are as follows: Mn²⁺ (0.83 Å) > Mn³⁺ (0.64 Å) > Ga³⁺ (0.62 Å) > Mn⁴⁺ (0.53 Å) [15], the slightly smaller inter-planar spacing of GMO-O₂ and the much larger inter-planar spacing of GMO-air indicate that more Mn⁴⁺

ions are incorporated in GMO-O₂ and more Mn²⁺ ions are incorporated in GMO-air, which will be quantitatively confirmed by the HRTEM and XPS results later.

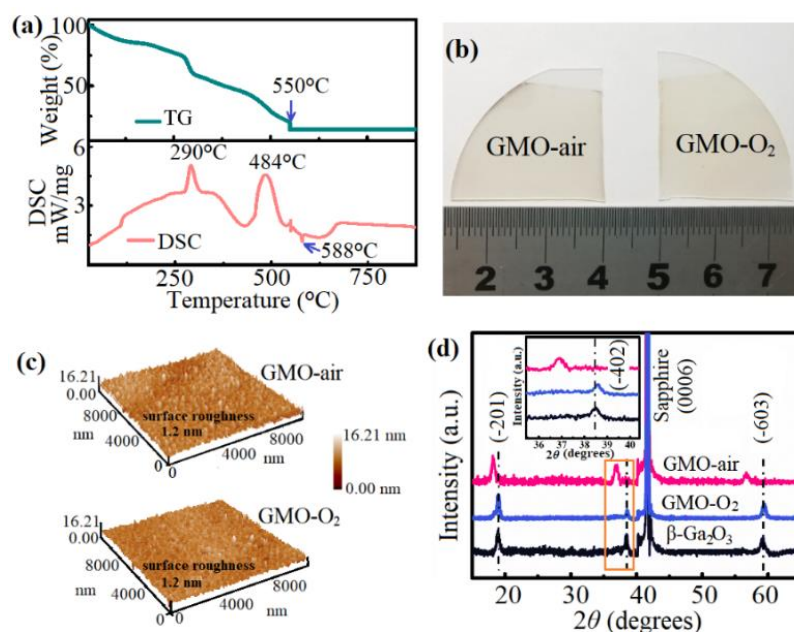


FIG. 1. (a) TG and DSC curves of the GaMn-polymers in the air. (b) The digital photos of the GMO films grown on the sapphire substrates. (c) 3D AFM images of the GMO films grown on the sapphire substrates. (d) XRD patterns of the PAD-grown GMO-air, GMO-O₂ and undoped β-Ga₂O₃ films on the *c*-plane sapphire. The inset is the enlarged view of XRD patterns around 38°.

The microstructures of the GMO films are then studied by HRTEM. The Cross-sectional HRTEM images of the GMO-air and GMO-O₂ films are shown in Figs. 2(a) and 2(c), respectively. The corresponding spherical aberration HRTEM images of the GMO-air and GMO-O₂ films are shown in Figs 2(b) and 2(d), respectively. Both the GMO-air and GMO-O₂ films are highly crystalline and grown along the direction of (-201), consistent with the XRD results. Clear crystalline structures can be seen and no Mn-related clusters or precipitates can be found in both cases. The inter-planar spacings

along (-402) azimuth of the GMO-air and GMO-O₂ films are about 0.240 nm and 0.230 nm, respectively, consistent with the XRD results.

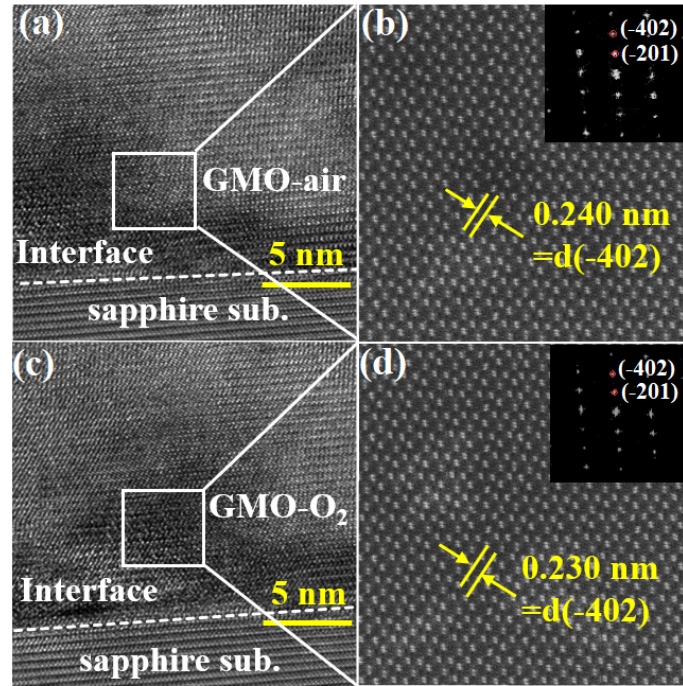


FIG. 2. (a) Cross-sectional high-resolution TEM image of GMO-air film. (b) Spherical aberration TEM image of GMO-air film. (c) Cross-sectional high-resolution TEM image of GMO-O₂ film. (d) Spherical aberration TEM image of GMO-O₂ film. The insets show the corresponding FFT.

To investigate the effect of annealing atmosphere on the chemical states of the elements, XPS measurements are performed on the GMO-air and GMO-O₂ films. By fitting the XPS whole scanning spectra (not shown), the atomic ratios between oxygen and cation of GMO-air and GMO-O₂ films are obtained as 1.42 and 1.45 respectively. The stoichiometric ratio is less than 1.5 in Ga₂O₃, indicating the existence of vacancies. As shown in Figs. 3(a) and (b), each O 1s peak of GMO-air and GMO-O₂ could be fitted into two sub-peaks located at 530.7 eV and 532.1 eV, corresponding to O ions

surrounded by metal atoms (O_{lat}) and V_{Os} in the metal bonding matrix, respectively [20,21]. The area ratio of V_{Os} -related peak of GMO-air and GMO- O_2 are estimated to be 30% and 18%, respectively, indicating that there are more V_{Os} in GMO-air. The Mn doping concentrations in GMO-air and GMO- O_2 both are about 34.5%, estimated by fitting the XPS whole scanning spectra (not shown). Figs. 3(c) and (d) show the Mn 2p spectra of the GMO-air and GMO- O_2 films, respectively. The main peak can be fitted into three sub-peaks located at about 640.6 eV, 641.8 eV and 643.2 eV, corresponding to Mn^{2+} , Mn^{3+} and Mn^{4+} ions, respectively [15,22]. The concentrations of Mn^{2+} , Mn^{3+} and Mn^{4+} ions in GMO-air are obtained as 13.9%, 14.6% and 6.0%, respectively, while the concentrations of Mn^{2+} , Mn^{3+} and Mn^{4+} ions in GMO- O_2 are 7.6%, 14.9% and 12.0%, respectively. The doping concentrations of different Mn ions and the area ratio of V_{Os} -related peak are shown in Fig. 3(f). Much more Mn^{2+} ions in GMO-air are responsible for the increase of inter-planar spacing shown in Fig. 1(d). Meanwhile, more Mn^{4+} ions in GMO- O_2 are responsible for the decrease of inter-planar spacing shown in Fig. 1(d). In general, substitutional Mn dopants in Ga_2O_3 mainly exist as Mn^{3+} ions when there are no other defects around [15]. When there is a V_O nearby a Mn^{3+} ion, two extra electrons are introduced in the β - Ga_2O_3 lattice, one of which enters the Mn d-shell and convert the Mn^{3+} ion into an Mn^{2+} ion [17,22]. When there is a gallium vacancy (V_{Ga}) nearby a Mn^{3+} ion, the V_{Ga} acts as an acceptor and captures a 3d electron from the Mn d-shell, converting the Mn^{3+} ion into an Mn^{4+} ion [17,22]. The schematic of formation of Mn^{2+} , Mn^{3+} and Mn^{4+} ions in the GMO films is shown in Fig. 3(e). It is worthwhile noting that this is the first time that Mn^{4+} ions are observed in Mn-doped

Ga₂O₃. Based on the assumption that one Mn⁴⁺ ion corresponds to one V_{Ga}, the higher concentration of Mn⁴⁺ ions in GMO-O₂ means higher V_{Ga} concentration in GMO-O₂, which is reasonable since pure O₂ provide more oxygen than air.

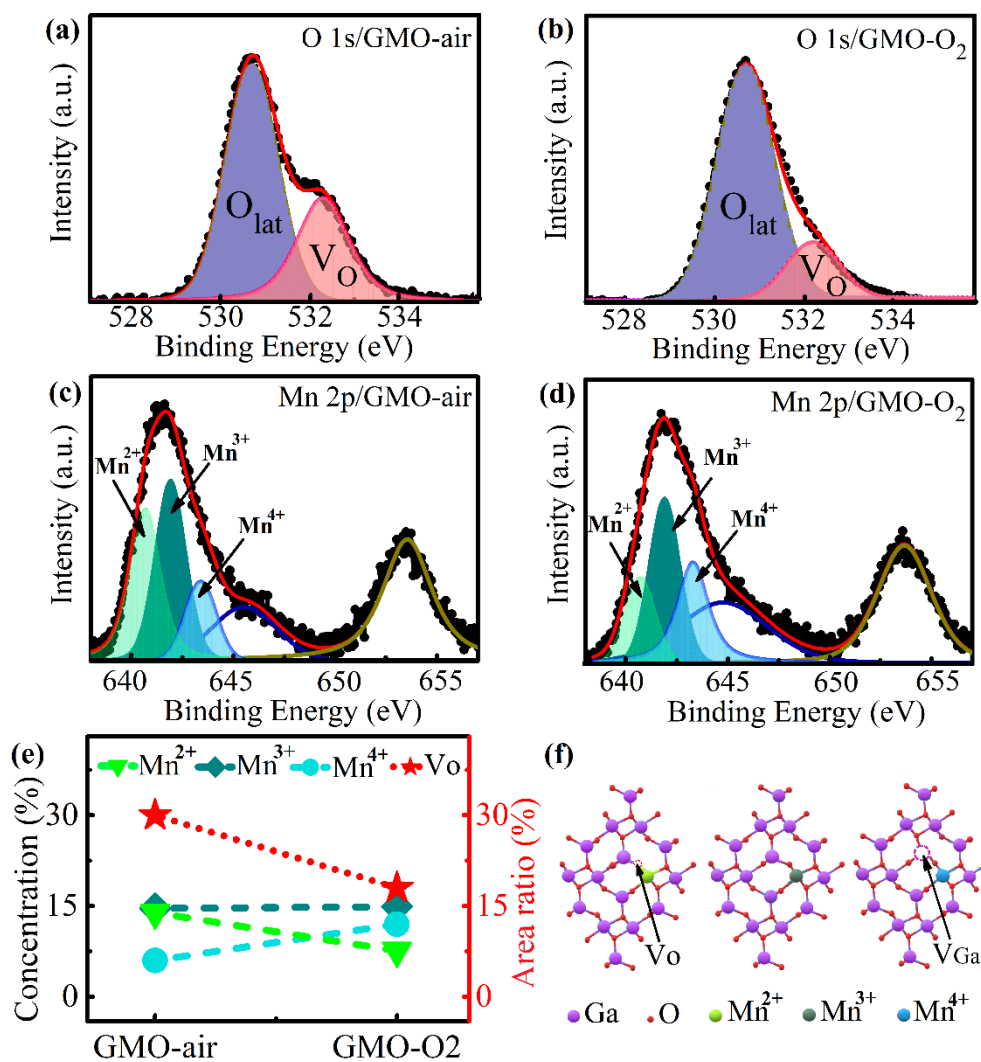


FIG. 3. O 1s peaks of (a) GMO-air and (b) GMO-O₂. Mn 2p peaks of (c) GMO-air and (d) GMO-O₂. (e) The doping concentrations of different Mn ions and the area ratio of V_O -related peak in the GMO films. (f) The schematic diagram of formation of Mn^{2+} , Mn^{3+} and Mn^{4+} ions in Ga₂O₃.

Figure 4(a) shows the optical transmittance measured by UV-visible spectrophotometer of the GMO films. The GMO-air film exhibits slightly lower optical

transmittance than that of the GMO-O₂ film, consistent with the results observed in Fig. 1(b). The inset is the $(\alpha h\nu)^2$ versus $h\nu$ plot of the GMO films. By fitting the plot of $(\alpha h\nu)^2$ versus $h\nu$, the band gaps of GMO-air and GMO-O₂ are obtained as 4.98 eV and 5.18 eV, respectively. It is more V_{OS} in GMO-air that results in lower optical transmittance and smaller band gap, owing to the contributions of more occupied defect levels [23,24]. Figure 4(b) shows the PL spectra of the GMO films measured at room temperature with an excitation wavelength of 250 nm. The emission band can be divided into four bands centered at about 345 nm, 415 nm, 440 nm and 480 nm, respectively. The ultraviolet emission band located at about 345 nm corresponds to the recombination of self-trapped excitons, which is an intrinsic process [25]. The emission peaks centered at 415 nm, 440 nm (violet region) and 480 nm (blue region) are originated from the electron-hole recombination formed by V_{OS}, or from the recombination of Ga-O vacancy pair [26,27]. The PL intensity at the violet and blue light regions of the GMO-air films are stronger than that of GMO-O₂ films, which can be attributed to more defects such as V_{OS} in the GMO-air films. The electrical measurements show that the resistivity values of the GMO-air and GMO-O₂ films are $1.2 \times 10^4 \ \Omega \cdot \text{cm}$ (n) and $9.1 \times 10^4 \ \Omega \cdot \text{cm}$, respectively, and the majority carriers are electrons (n-type), which can be roughly explained by the fact that more V_{OS} exist in GMO-air films since V_{OS} act as donor-type defects to provide electrons in Ga₂O₃. In short, the large difference between the V_O concentrations in the GMO-air and GMO-O₂ films results in the tuning of the optical and electrical properties.

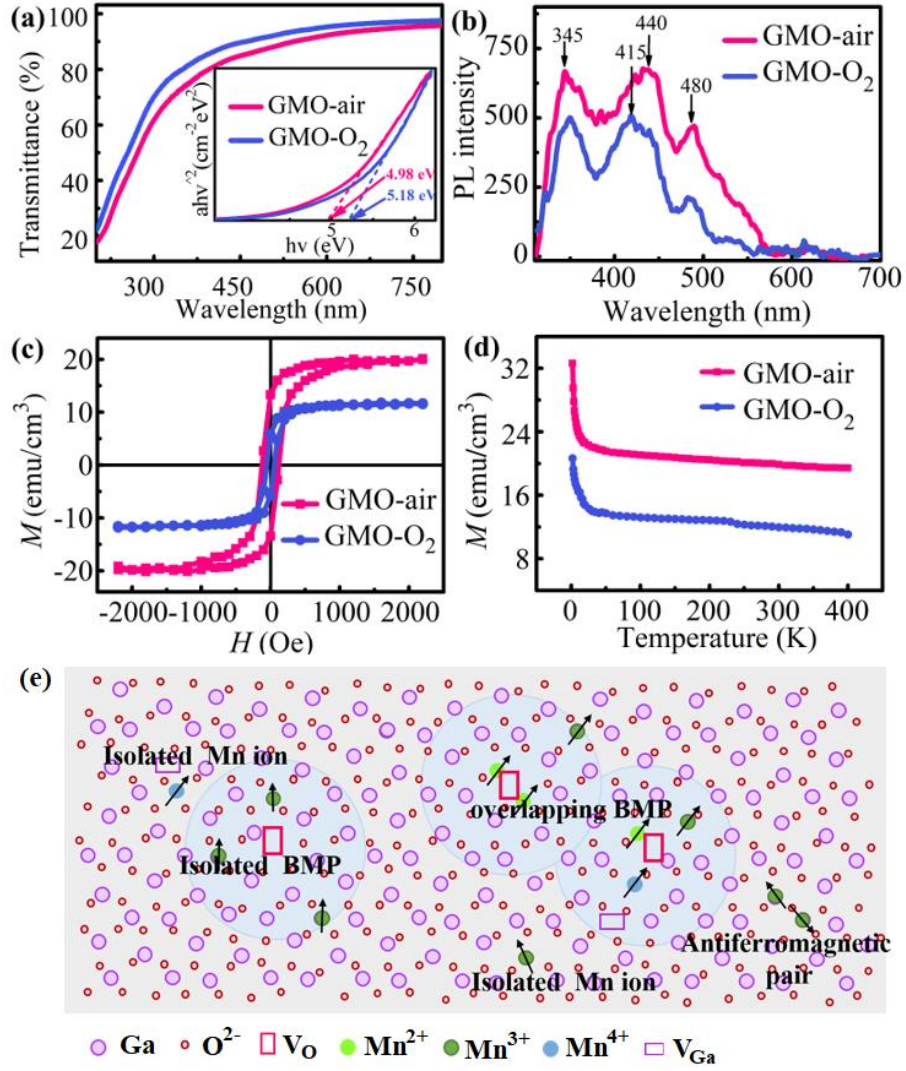


FIG. 4. (a) Optical transmittance spectra of the GMO films. Inset is the $(\alpha h\nu)^2$ versus $h\nu$ plot. (b) Room-temperature PL spectra of the GMO films excited at 250 nm. (c) M - H curves of the GMO films at 300 K. (d) Temperature-dependent magnetization of the GMO films. (e) Schematic of bound magnetic polarons in the GMO films.

Figure 4(c) shows the magnetization versus magnetic field (M - H) curves of the GMO films obtained at 300 K, in which H is swept in plane since the easy magnetic axis of the films is in-plane [16]. Both GMO films display typical hysteresis loops, which are clear signals of ferromagnetism. The M_S values of the GMO-air and GMO-O₂ films are 19.7 emu/cm³ and 11.6 emu/cm³, corresponding to magnetic moments of 0.09 μ_B /Mn

and 0.05 $\mu\text{B}/\text{Mn}$, respectively. The H_C values of the GMO-air and GMO-O₂ films are 120 Oe and 58 Oe, respectively. Obviously, GMO-air exhibits stronger M_S and H_C values, 1.7 and 2.1 times those of GMO-O₂, respectively. The temperature-dependent magnetization (M - T) curves of the GMO-air and GMO-O₂ films measured in field-cooling mode under 2000 Oe are shown in Fig. 4(d), which are clearly indicative of ferromagnetism up to temperatures higher than 400 K. The magnetizations of both samples increase very slowly from 400 K down to 20 K, and then increase steeply at temperatures lower than 20 K, which is also observed in Mn-doped γ -Ga₂O₃ and ascribe to the presence of paramagnetic components inducing additional magnetization at low temperatures [18]. Notably, the M - T curves also reveal stronger magnetization in GMO-air films.

To understand the difference between the ferromagnetic properties in GMO-air and GMO-O₂, we should point out that the ferromagnetism comes from bound magnetic polarons (BMPs) [28] which are closely related to the defects in the GMO films. As we know, a V_O acts as a donor and provides two additional electrons in the β -Ga₂O₃ lattice, which are confined in hydrogenic orbitals [29]. When the donor concentration exceeds a critical concentration, the hydrogenic orbitals overlap to form impurity energy bands, making the localized hydrogenic electrons become delocalized. The overlap between delocalized hydrogenic electrons and Mn ions with local spin moments within the hydrogenic orbitals will lead to ferromagnetic exchange coupling between them and form BMPs [29], as shown Fig. 4(e). When the number of BMPs reaches a certain concentration, percolation occurs and ferromagnetic ordering is produced. It is noted

that the Mn ions not included in hydrogenic orbitals will not participate in creating long-range ordered ferromagnetic coupling. In addition, V_{Ga} may produce weak local spin moments, but it is difficult for them to form stable long-range magnetic ordering [8]. Therefore, the ferromagnetism depends on the concentration of V_{Os} and Mn ions that are coupled with each other. According to Hund's rule, the spins contributed by an Mn^{2+} , an Mn^{3+} and an Mn^{4+} ion are 4/2, 5/2 and 4/2, respectively [29,30]. In other words, an Mn^{2+} and an Mn^{4+} ion provide the same local magnetic moment, while an Mn^{3+} ion provides more local magnetic moment than the other two ions. Interestingly, GMO-air and GMO- O_2 have approximately the same concentration of Mn^{3+} ions and same concentration of total Mn dopants. This means that, if the V_O concentration was high enough so that all the Mn ions were included in hydrogenic orbitals, GMO-air and GMO- O_2 would exhibit the same magnetization, which is not the case in our work. In fact, the concentration of Mn ions in the GMO films is as high as 34.5%, much higher than the V_O concentration. In this situation, the magnetization is determined by the V_O concentration instead of the concentration of Mn ions. Thus, the stronger magnetization in GMO-air can only be ascribed to more V_{Os} in it. Notably, the area ratio of V_{Os} -related peak in GMO-air over that of GMO- O_2 is 1.7, quantitatively consistent with the ratio (1.7) of the M_s of GMO-air over that of GMO- O_2 . In addition, the greater H_C value in the GMO-air films is ascribed to more V_{Os} , since the H_C value increases with the increase of pinning sites originated from the V_{Os} in oxide films [31,32]. Therefore, it is the different annealing atmospheres that modulate the magnetizations in the GMO films by engineering the concentrations of V_{Os} .

IV. CONCLUSIONS

The GMO films with RTFM are prepared by PAD and the effects of annealing atmosphere on their structures and physical properties are studied. Our results show that M_s of GMO-air is 1.7 times that of GMO-O₂, closely correlated with the ratio (1.7) of the V_O concentration in GMO-air over that of GMO-O₂. This correlation can be explained by defect-controlled ferromagnetism in terms of the BMP model and the variation of concentrations of V_Os and various Mn ions (Mn²⁺, Mn³⁺, and Mn⁴⁺ ions) due to annealing. In addition, the optical and electrical properties of the samples are also modulated. Our results provide insights into the defect-controlled ferromagnetism in β -Ga₂O₃ and may be useful for related electronic and spintronic applications.

ACKNOWLEDGMENT

We are grateful to the National Natural Science Foundation of China (Grant No. 52172272). We would like to thank the Analytical & Testing Center of Sichuan University for the XRD and XPS measurements.

- [1] S. Fusil, V. Garcia, A. Barthélemy, and M. Bibes, *Annu. Rev. Mater. Res.* 44, 91 (2014) .
- [2] P. Dorpe, Z. Liu, W. Roy, V. Motsnyi, M. Sawicki, G. Borghs, and J. De Boeck, *Appl. Phys. Lett.* 84, 3495 (2004) .
- [3] Z. Li, W. Bai, Y. Li, Y. Li, S. Wang, W. Zhang, J. Zhao, Z. Sun, C. Xiao, and Y. Xie, *Sci. China Mater.* 65, 780 (2021).
- [4] Y. Liu, G. Wang, S. Wang, J. Yang, L. Chen, X. Qin, B. Song, B. Wang, and X. Chen, *Phys. Rev. Lett.* 106, 087205 (2011).

- [5] W. Kong, G. Wu, K. Wang, T. Zhang, Y. Zou, D. Wang, and L. Luo, *Adv. Mater.* 28, 10725 (2016).
- [6] M. Higashiwaki, K. Sasaki, H. Murakami, Y. Kumagai, A. Koukitu, A. Kuramata, T. Masui, and S. Yamakoshi, *Semicond. Sci. Tech.* 31, 034001 (2016).
- [7] M. Passlack, M. Hong, J.P. Mannaerts, R.L. Opila, and F. Ren, *Appl. Phys. Lett.* 69, 302 (1996).
- [8] Y. Yang, J. Zhang, S. Hu, Y. Wu, J. Zhang, W. Ren, and S. Cao, *Phys. Chem. Chem. Phys.* 19, 28928 (2017).
- [9] Y. Huang, A. Gao, D. Guo, X. Lu, X. Zhang, Y. Huang, J. Yu, S. Li, P. Li, and W. Tang, *J. Mater. Chem. C* 8, 536 (2020).
- [10] S. Ye, Y. Zhang, H. He, J. Qiu, and G. Dong, *J. Mater. Chem. C* 3, 2886 (2015).
- [11] D. Guo, Z. Wu, P. Li, Q. Wang, M. Lei, L. Li, and W. Tang, *Rsc. Adv.* 5, 12894 (2015).
- [12] E. Chikoidze, H. Bardeleben, K. Akaiwa, E. Shigematsu, K. Kaneko, S. Fujita, and Y. Dumont, *J. Appl. Phys.* 120, 025109 (2016).
- [13] B. Peng, Y. Zhang, Y. Wang, L. Yuan, L. Dong, and R. Jia, *J. Magn. Magn. Mater.* 506, 166687 (2020).
- [14] G. Pei, C. Xia, Y. Dong, B. Wu, T. Wang, and J. Xu, *Scripta Mater.* 58, 943 (2008).
- [15] D. Guo, Z. Wu, Y. An, X. Li, X. Guo, X. Chu, C. Sun, L. Ming, L. Li, and L. Cao, *J. Mater. Chem. C* 3, 1830 (2015).
- [16] Y. Huang, Z. Chen, X. Zhang, X. Wang, Y. Zhi, Z. Wu, and W. Tang, *J. Semicond.* 39, 053002 (2018).

- [17] X. Wang, R. Quhe, Y. Zhi, Z. Liu, X. Dai, Y. Tang, Z. Wu, and W. Tang, Superlattice. Microst. 125, 330 (2019).
- [18] H. Hayashi, H. Rong, H. Ikeno, F. Oba, S. Yoshioka, I. Tanaka, and S. Sonoda, Appl. Phys. Lett. 89, 181903 (2006).
- [19] Q.X. Jia, T.M. Mccleskey and A.K. Burrell, Nat. Mater. 3, 529 (2004).
- [20] X. Dai, Q. Zheng, X. Zhang, Y. Wang, and G. Xiang, Mater. Lett. 284, 1 (2021).
- [21] C. C. Yang, J. Q. Huang, K. Y. Chen, P. H. Chiu, H. T. Vu, and Y. K. Su, IEEE Access 7, 175186 (2019).
- [22] D. Guo, P. Li, Z. Wu, W. Cui, X. Zhao, M. Lei, and L. Li, Sci. Rep-UK 6, 24190 (2016).
- [23] H. Liu, F. Zeng, Y. Lin, and G. Wang, Appl. Phys. Lett. 102, 041301 (2013).
- [24] Q. Zhou, X. Tao, G. Di, Y. Shang, and L. Dong, Energ. Fuel. 35, 5101 (2021).
- [25] S. Rafique, L. Han, and H. Zhao, Phys. Status Solidi A 214, 1700063.1 (2017).
- [26] L. Binet, and D. Gourier, J. Phys. Chem. Solids 59, 1241 (1998).
- [27] K. W. Chang, and J. J. Wu, Adv. Mater. 16, 545 (2004).
- [28] A. C. Durst, A. C. Durst, R. N. Bhatt, and P. A. Wolff, Phys. Rev. B **65**, 2352051 (2002).
- [29] J. M. D. Coey, M. Venkatesan, and C. B. Fitzgerald, Nat. Mater. **4**, 173 (2005)
- [30] F. López-Urías and A. Díaz-Ortiz, J. Alloys Compd. **369**, 117 (2004).
- [31] S. Singh and N. Khare, Appl. Surf. Sci. 364, 783 (2016).
- [32] J. ping Zhou, H. cai He, and C. W. Nan, Appl. Surf. Sci. 253, 7456 (2007).